Chapter 5 Evidence for Four Spin-Glass Transitions in $BaFe_{12}O_{19}$ due to Successive Freezing of Transverse and Longitudinal Spin Components

5.1 Introduction

In the preceding two chapters, we presented results of X-ray absorption spectra (XAS) and X-ray magnetic circular dichroism (XMCD) from 1.2 K to 30 K, single-crystal neutron diffraction studies at 1.5 K and dc magnetization M(T) studies in the temperature range 2 to 950 K on single crystals of $BaFe_{12}O_{19}$ (BFO). The four main findings of these studies are: (1) The $3dFe^{3+}$ spin magnetic moment in BFO are canted with respect to the crystallographic c-axis giving rise to longitudinal conical magnetic order which is incommensurate with respect to the underlying lattice. (2) The component of the spin magnetic moment in the basal plane, obtained by XMCD studies, decreases with temperature below 30 K until it takes an upturn around 15 K. This behaviour was confirmed by dc magnetisation studies also. (3) It was also shown that the band width of the e_g energy levels also change around 15 K suggesting that the strength of the exchange-correlations is changing around this temperature. (4) The magnetocrystalline anisotropy A ($\frac{M_{\perp c}}{M_{//c}}$) in the dc magnetization studies increases with decreasing temperature below T_c and peaks around 45 K suggesting significant canting of spins even above 30 K upto which the XMCD studies were carried out.

In a related M-type hexaferrite material with magnetoplumbite structure, $SrCr_8Ga_4O_{19}$ (SCGO), with a maximum Ga content of ~33.3% in the magnetic sublattice, it has been shown that the spins lie entirely in the ab-plane and not along the c-axis, in marked contrast to the Gorter model for the isostructural Ba-hexaferrite [237]. The SCGO has received enormous attention [17,18,152,238–242,19,21–27] of the exotic spin

liquid [18,24,27] and spin-glass [17–19,21–26] transitions as a function of Ga content in the magnetic sublattice due to the formation of kagome bi-layer type stacking of the spins which are completely frustrated [19,21,237]. The presence of a significant component of the spins in the ab-plane, discussed in chapters 3 and 4, raises the possibility of the formation of geometrically frustrated kagome bi-layer configuration of the spins in the ab-plane of BFO also similar to that reported in the context of SCGO [19,237]. This calls for revisiting the nature of the magnetic transitions in BFO also, especially the magnetic transition seen in the dc M(T) around ~ 45 K at 500 Oe, discussed in the previous chapter, and observed by previous workers also [137] has a spin-glass character as a result of geometrically frustrated nature of the basal plane component of the spins in a way similar to that observed in the SCGO system [18,19]. Further, the change in the exchange-correlation energy around 15 K may drive additional magnetic transitions in BFO at low temperatures.

Taking the cue from the dc M(T), XAS and XMCD studies discussed in chapter 4, we have carried out alternating current (ac) magnetic susceptibility measurements as a function of temperature and frequency ($\chi(\omega, T)$) in the 2 to 300 K range to explore the magnetic transitions in BFO below the room temperature. In addition, we have also carried out neutron diffraction measurements as function of temperature in the 2 to 300 K on BFO single crystals to seek signatures of the magnetic transitions at low temperatures observed in $\chi(\omega, T)$ measurements. The analysis of the temperature (T) and frequency dependent real (χ') and imaginary (χ'') parts of ac susceptibilities $\chi_{\perp c}(\omega, T)$ and $\chi_{//c}(\omega, T)$ carried out with an ac drive field applied perpendicular ($\perp$) and parallel (//) to the c-axis of the BFO single-crystals, respectively, are presented in this chapter. It reveals occurrence of four spin-glass (SG) transitions involving spin components perpendicular ($\perp$) and parallel (//) to the c-axis with critical spin-glass transition temperatures at which

the spin relaxation dynamics diverges due to ergodicity breaking as $T^{1}_{SG\perp c} \simeq 46$ K and $T^{4}_{SG\perp c} \simeq 4$ K in the ab-plane and $T^{2}_{SG//c} \simeq 25$ K and $T^{3}_{SG//c} \simeq 15$ K along the c-axis. We also present evidence for the signature of these spin-glass transitions in the variation of the integrated intensities of the *006* and *101* reflections as a function of temperature using single-crystal neutron diffraction measurements. It is shown that the successive spin-glass phases in BFO coexist with the long-range ordered (LRO) ferrimagnetic phase and only a part of the longitudinal (//c) and transvesrse ($\perp$c) components of the spins takes part in spin-glass freezing. This is the first report of four spin-glass transitions in any ordered or disordered system

5.2 Experimental

Single crystals were grown using high-temperature flux method using pre-calcined powders and a flux, the details of which are given in chapter 2. The $M_{\perp c}(T)$ measurements were carried out using a SQUID-based magnetometer (MPMS-3, Quantum Design, USA). The $M_{\perp c}(T)$ measurements on zero-field cooled (ZFC) and field cooled (FC) crystals were carried out during the warming cycle under a dc magnetic field of 500 Oe. The frequency-dependent ac-susceptibility $\chi_{\perp c}(\omega, T)$ and $\chi_{//c}(\omega, T)$ measurements on the same single crystals were carried out under an ac drive field of 3 Oe applied perpendicular and parallel to the c-axis, respectively, using the same MPMS-3 set-up. The relaxation of thermoremanent magnetization (TRM) was investigated for the $M_{\perp c}(t)$ measurements carried out with a magnetic field 1000 Oe applied perpendicular to c-axis at a temperature below transverse spin-glass transition temperature ($T_{SG\perp c} \sim 46$ K) using a physical properties measurement system (PPMS, DynaCool, Quantum Design, USA).

The temperature-dependent neutron diffraction measurements on single-crystals of BFO were carried out using WISH time-of-flight diffractometer at ISIS facility of the Rutherford Appleton Laboratory (RAL), United Kingdom, the details of which are

available elsewhere [209]. Mantid software [243] was used to analyse the neutron scattering data.

5.3 Magnetic Susceptibility Studies

5.3.1 Evidence for the Freezing of the Transverse Component of the Spins

The observation of significant component of spins in the ab-plane of BFO in M(T) and XMCD studies discussed in chapter 4, and occurrence of the magnetic transition around ~ 45 K in the $M_{\perp c}$(T) plot suggests that this transition may have a spin-glass character in analogy with the spin-glass transition in SCGO [19]. To verify this, we first measured $M_{\perp c}$(T) during the warming cycle on zero-field cooled (ZFC) and field cooled (FC) single-crystals and one typical result is depicted in Fig. 5.1(a). Evidently, $M_{\perp c}$(T) exhibits irreversibility between the ZFC and FC magnetization curves below T_{irr} $\lesssim$ 80 K as revealed by the bifurcation of the two curves in the figure. Such an irreversibility of the ZFC and FC magnetization curves can occur either due to blocking of non-interacting spin clusters as in superparamagnetic (SPM) systems [244] or due to the onset of non-ergodic behaviour due to an impending spin-glass transition [57–61,245–247].

The decay of thermoremanent magnetization (TRM) for $M_{\perp c}$(t) was investigated on a BFO single crystals cooled from 300 K to 40 K under a field of 1000 Oe and then held at this temperature for 600 sec in the presence of the same dc magnetic field (i.e., H = 1000 Oe) applied perpendicular to the c-axis. After the elapse of 600 sec, the magnetic field was switched off and the decay of magnetization $M_{\perp c}$(t) as a function of time (t) was recorded for 8 hours. Fig. 5.1(b) depicts the time evolution of $M_{\perp c}$(t) for one typical measurement. The decay of TRM in spin-glass systems is known to follow Kohlrausch-Williams-Watt (KWW) type stretched exponential behaviour [57,60,74,75,248–252]:

$$M(t) = M_0 + M_g \exp\{-(t/\tau_r)^{\beta}\}, \qquad \text{.....(5.1)}$$

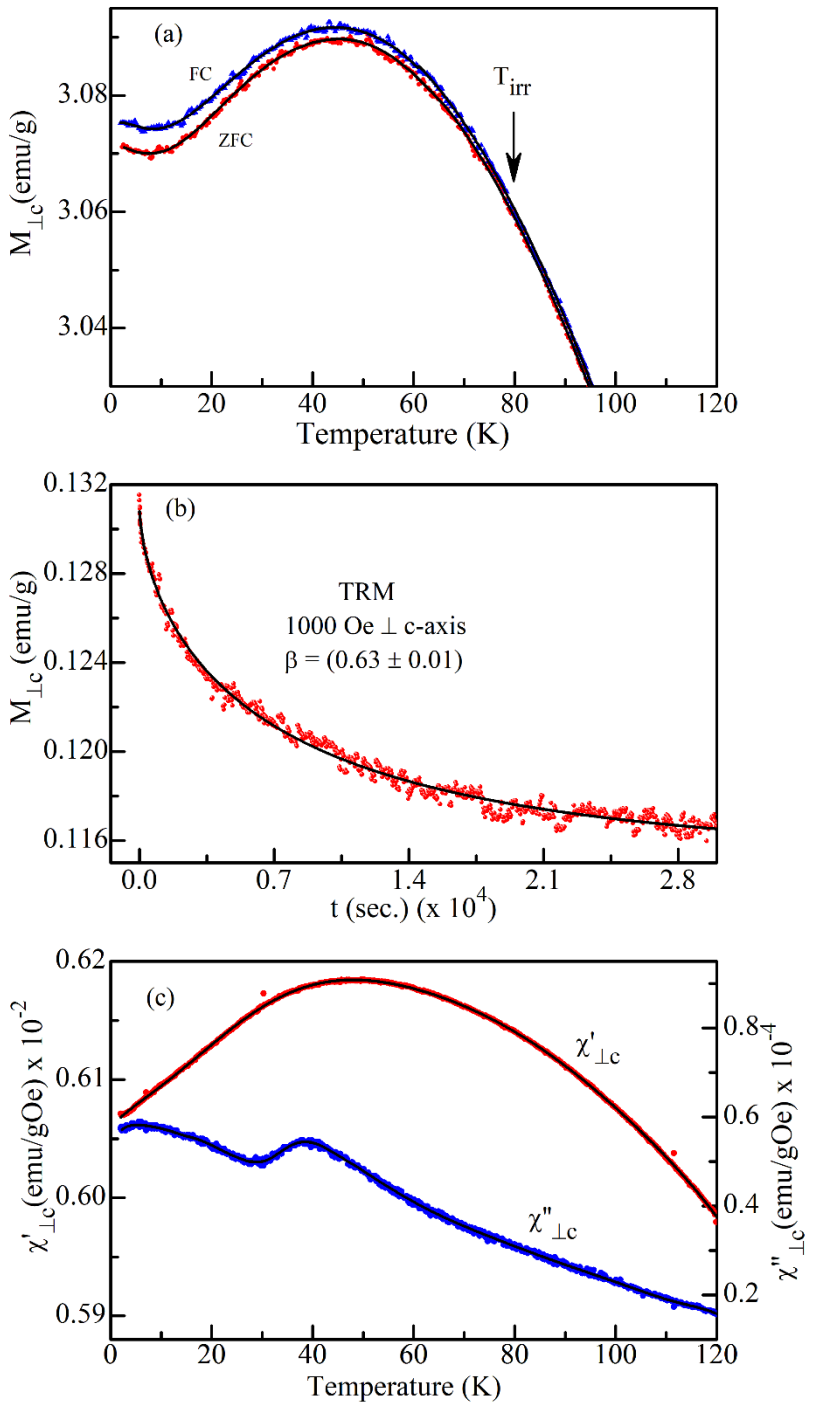

Figure 5.1: (a) Variation of the ZFC and FC magnetization ($M_{\perp c}$) measured with dc field of 500 Oe applied perpendicular to the c-axis of the crystal. (b) Evolution of thermoremanent magnetization $M_{\perp c}(t)$ of a 1000 Oe FC crystal with time at 40 K. (c) Temperature dependence of real $\chi'_{\perp c}$ and imaginary $\chi''_{\perp c}$ parts of the ac susceptibility measured at 545 Hz with an ac field drive of 3 Oe applied perpendicular to the c-axis of the crystal.

where M_0 is the ferromagnetic component due to the coexistence of ferrimagnetic phase with the spin-glass phase, M_g is the glassy component and τ_r is the characteristic relaxation time. For $\beta = 1$, the system follows exponential decay, $M(t) = M_0 + M_g\exp\{-t/\tau_r\}$, with a single relaxation time (τ) corresponding to the potential energy barriers of equal height. Since the energy landscape for spin-glass systems is multivalleyed with different barrier heights, the relaxation time (τ) has a distribution [57,60,251] and this situation has been modelled using stretched exponential function given by Equation (5.1) where β lies in the range $0 < \beta < 1$due to the distribution of τ [57,60,248–251]. A least-squares fit using the KWW function (Equation (5.1)) gives an excellent fit between the observed and calculated $M_{\perp c}(t)$ with $M_0 = (0.115 \pm 0.0001)$ emu/g, $M_g = (0.015 \pm 0.00018)$ emu/g, $\tau_r = (7415 \pm 2)$ sec and $\beta = (0.63 \pm 0.01)$. The value of $\beta = 0.63$ rules out the possibility of relaxation of TRM due to purely long-range ordered ferrimagnetic phase of BFO, for which β should have been equal to 1, and suggests the presence of metastable states in the system, possibly due to its glassy nature [251].

To resolve whether the irreversibility of ZFC and FC M(T) and non-exponential decay of TRM is due to SPM blocking or spin-glass freezing, we first present the result of ac-susceptibility $\chi(\omega, T)$ measurements using an ac drive field of 3 Oe applied in a direction transverse to the c-axis of the BFO crystals. The corresponding temperature variation of $\chi'_{\perp c}$ and $\chi''_{\perp c}$ is shown in Fig. 5.1(c) for a frequency of 545 Hz. It is evident from this figure that $\chi'_{\perp c}$ exhibits a peak around ~ 48 K while $\chi''_{\perp c}$ exhibits a peak at T ~ 38 K. For long-range ordered (LRO) magnetic transitions, both $\chi'(\omega, T)$ and $\chi''(\omega, T)$ should peak at the same temperature as per the Kramer-Koning relationship [253] that relates the two quantities. The fact that the peak temperatures $T_f'(\omega)$ and $T_f''(\omega)$ corresponding to the peaks in $\chi'(\omega, T)$ and $\chi''(\omega, T)$, respectively, are not coincident with

$T_f''(\omega) < T_f'(\omega)$ suggests that this transition may not be a long-range ordering type. In addition, the $\chi''_{\perp c}(\omega, T)$ plot in Fig. 5.1(c) shows another peak at ~ 5 K. This transition appears to be a rather weak transition as there is no obvious signature of this transition in $\chi'(\omega, T)$ plot but its signature in the $\chi''(\omega, T)$ plot is quite unambiguous. We believe that the signature of this transition in $\chi'(\omega, T)$ is overwhelmed by the higher temperature transition which is a strong transition with prominent signature in $\chi'(\omega, T)$ and $\chi''(\omega, T)$ plots. However, the signature of both the transitions are seen in the neutron diffraction studies discussed in a latter section. In order to understand the nature of these two transitions, we measured the $\chi'_{\perp c}(\omega, T)$ and $\chi''_{\perp c}(\omega, T)$ plots at different frequencies ($\omega = 2\pi f$) and the results are shown in Figs. 5.2(a) and (b), respectively. It is evident from this figure that both the peak temperatures, i.e., $T_f'(\omega)$ and $T_f''(\omega)$, shift towards the higher side with increasing measuring frequency as expected for the spin-glasses [57–61,245–247] as well as the SPM [244] systems. The smaller peak seen in $\chi''_{\perp c}(\omega, T)$ (Fig. 5.1(c)) has been magnified in Fig. 5.2(c) to demonstrate the frequency dispersion of $T_f''(\omega)$ for this transition also.

For the SPM blocking transition, the temperature dependence of the spin relaxation time τ is known to follow Arrhenius behaviour [244]:

$$\tau(T) = \tau_0 \exp\left(\frac{E_a}{k_B T_f}\right), \qquad \text{.....(5.2)}$$

where τ_0 is the attempt relaxation time, E_a is the activation energy barrier and k_B is the Boltzmann constant. For spin-glass systems, the spin dynamics, on the other hand, shows critical slowing down following Vogel-Fulcher law [254] and/or a power law [57,60] behaviour:

Vogel-Fulcher law:

$$\tau(T) = \tau_0 \exp\left(\frac{E_a}{k_B(T_f - T_{VF})}\right), \qquad \text{.....(5.3)}$$

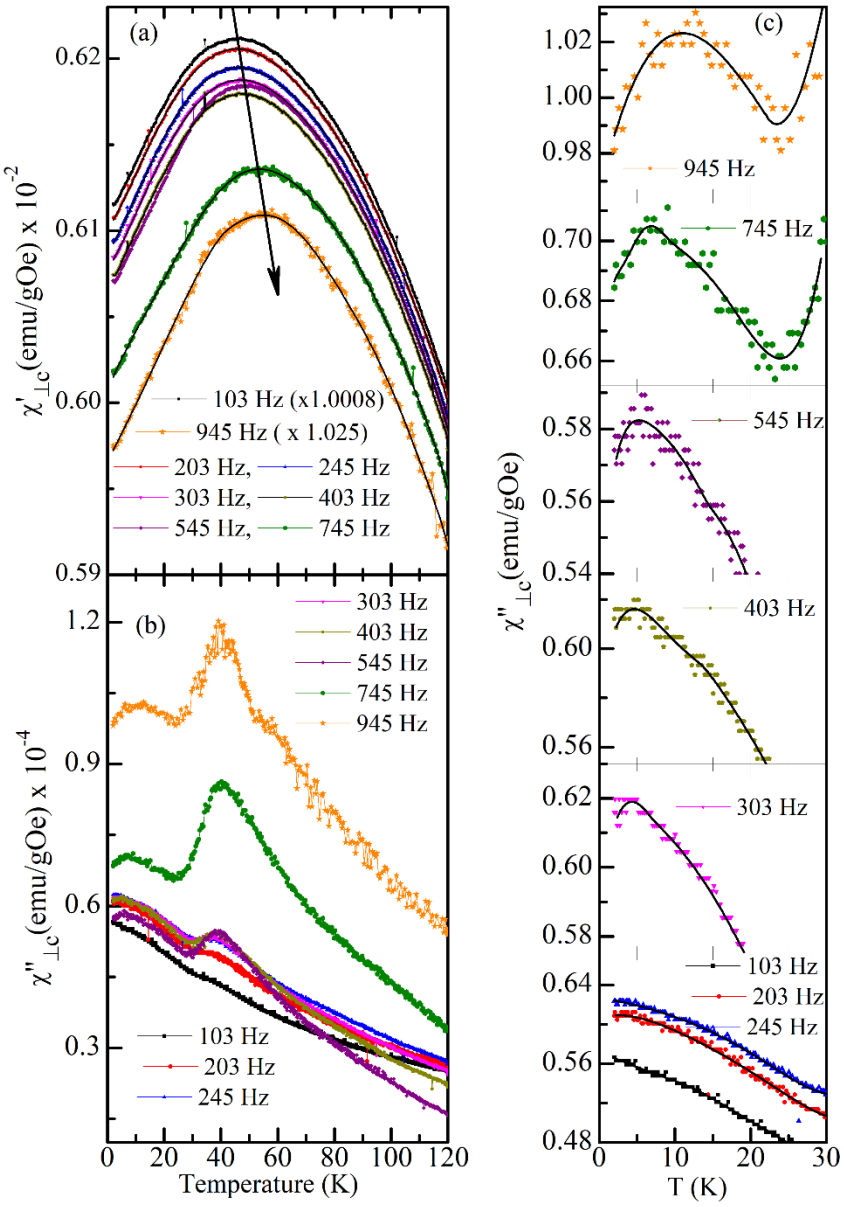

Figure 5.2: Temperature dependence of (a) real $\chi'_{\perp c}(\omega, T)$ and (b) imaginary $\chi''_{\perp c}(\omega, T)$ parts of ac susceptibility measured at various frequencies using an ac drive field of 3 Oe applied perpendicular to c-axis of the crystal; (c) depicts the lower temperature anomaly in $\chi''_{\perp c}(\omega, T)$ on a zoomed scale. The solid continuous lines through the data points in (c) are the fitted curves.

Power law:

$$\tau(T) = \tau_0 \left(\frac{(T_f - T_{SG})}{T_{SG}}\right)^{-zv}, \qquad \text{.....(5.4)}$$

where τ_0 is the inverse of the attempt frequency or attempt relaxation time, E_a is the activation energy, k_B is the Boltzmann constant, T_f is the frequency dependent peak temperature in $\chi'(\omega, T)$ or $\chi''(\omega, T)$, T_{VF} and T_{SG} are the critical Vogel-Fulcher and spin-glass transition temperatures, respectively, at which the relaxation time (τ) diverges as a result of ergodic symmetry breaking, z is the exponent for the power-law dependence of the correlation length ξ on τ (i.e., $\xi \sim \tau^{-z}$) while ν is the exponent for the temperature dependence of ξ (i.e., $\xi \sim ((T_f - T_{SG})/T_{SG})^{\nu}$) as per the scaling theories [57,60].

We first present the results of the analyis of $T_f'(\omega)$ for the higher tempeature transition. The relaxation time τ was taken as $1/\omega$, where $\omega = 2\pi f$ and f is the measuring frequency, corresponding to the peak temperature $T_f'(\omega)$ [60,255–257]. For the SPM blocking transition with Arrhenius behaviour, the $\ln(\tau)$ versus $1/T_f'$ plot should be linear. The non-linear nature of $\ln(\tau)$ versus $1/T_f'$ curve shown in Fig. 5.3 rules out the possibility of SPM blocking being responsible for the irreversibility of the ZFC and FC $M_{\perp c}(T)$ curves as well as the frequency dispersion of $T_f'(\omega, T)$. We then fitted the $\ln(\tau)$ versus $1/T_f'$ plots in Figs. 5.3 using Vogel-Fulcher law. The least-squares fit for the Vogel-Fulcher law shown using continuous solid line in Fig. 5.3 is in excellent agreement with observed data points suggesting that the higher temperature transition seen in $M_{\perp c}(T)$ and $\chi'_{\perp c}(\omega, T)$ is due to a spin-glass transition. The least-squares fitting parameters are: T'_{VF} = (45.46 ± 003) K, τ_0 = (1.8 ± 0.1) x 10^{-4} s, E_a = (0.13 ± 0.006) meV with a goodness of fit (GoF) of 0.995.

We also modelled the temperature dependence of τ using the power-law. The Equation (5.4) for the power-law dependence of τ on temperature can be written as:

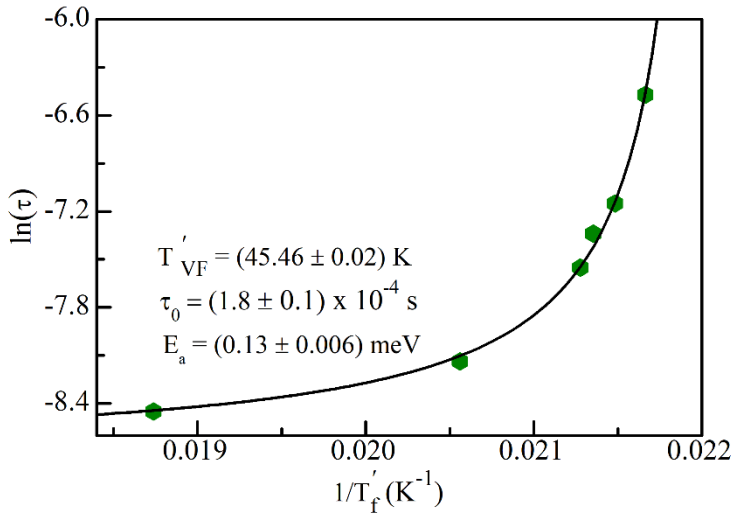

Figure 5.3: Variation of the ln(τ) with $1/T_f'$. The continuous solid line through the data points is the result of the least-squares fit for Vogel-Fulcher law using $\chi'(\omega, T)$ data.

$$\ln(\tau) = -(z\nu)\ln((T_f - T_{SG})/T_{SG}) + \ln(\tau_0), \qquad \text{.....(5.5)}$$

which is the equation of a straight line of the type

$$y = mx + c, \qquad \text{.....(5.6)}$$

where $y = \ln(\tau)$, $c = \ln(\tau_0)$, $m = -z\nu$, and $x = \ln((T_f - T_{SG})/T_{SG})$. Since there are three unknowns in Equation (5.5) ($z\nu$, τ_0, and T_{SG}) whereas only two unknowns can be determined using least-squares straight-line fit as per Equation (5.6), we followed the procedure given in ref. [258]. In this approach, one chooses different values of T_{SG}' and carries out least-squares fit for $\ln(\tau)$ vs $\ln((T_f' - T_{SG}')/T_{SG}')$ where the prime superscript signifies that these correpond to $\chi'_{\perp c}(\omega, T)$ data. The variance (σ) obtained for each value of T_{SG} by least-squares fit is plotted as a function of T_{SG} in Fig. 5.4(a). It is evident from this figure that σ shows a minimum corresponding to T_{SG}' = (46.035 ± 0.005) K. The range of uncertainty ± 0.005 K in the determination of the critical transition spin-glass transition temperature corresponds to the smallest interval at which we chose T_{SG} values

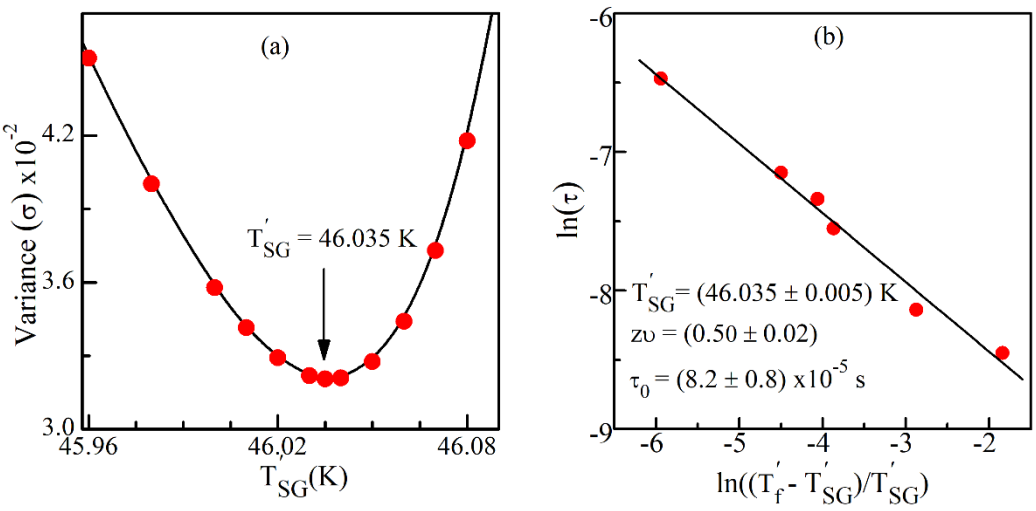

Figure 5.4: (a) Optimization of T'_{SG}. The minimum in (a) corresponds to the lowest variance with T'_{SG} ~ 46.035 K. (b) The least-squares fit for the power-law for ln(τ) versus $\ln((T'_f - T'_{SG})/T'_{SG})$ plot using $\chi'(\omega, T)$ data.

to determine the optimum one with the lowest variance. In this way, we obtained the best fit value of T'_{SG} = (46.035 ± 0.005) K. Using this optimised value of T'_{SG}, the least-squares fit for the ln(τ) versus $\ln((T'_f - T'_{SG})T'_{SG})$ was carried out and the resulting plot is depicted in Fig. 5.4(b). The fitting parameters for the best fit are: τ_0 = (8.2 ± 0.8) x 10^{-5} s, zν = (0.50 ± 0.02) and GoF = 0.984. Evidently both Vogel-Fulcher and power laws give comperable GoF and both confirm the divergence of the spin dynamics at T'_{VF}/T'_{SG} expected for a spin-glass transition due to ergodic symmetry breaking.

Since the signature of the lowest temperature transition is present only in the imaginary part $\chi''_{\perp c}(\omega, T)$ of the ac susceptibility, we also analysed the $\chi''_{\perp c}(\omega, T)$ data to verify if the divergence of the spin dynmics can be confirmed using $\chi''_{\perp c}(\omega, T)$ data as well for both the transitions. The spin relaxation time (τ) at various temperatures was obtained from the position of the peak in $\chi''_{\perp c}(\omega, T)$, i.e., $T''_f(\omega)$, using ωτ = 1 criterion as usual [60,259,260]. In the literature, the spin dynamics related to SPM blocking (T_B) and spin-glass transitions has been investigated using both $\chi'(\omega, T)$ and $\chi''(\omega, T)$ data [261–

264]. The non-linear nature of the the ln(τ) versus $1/T_f''$ plots shown in Figs. 5.5(a) and (b) for the higher and lower temperature transitions once again rules out the possibility of SPM blocking for frequency dispersion in $T_f''(\omega, T)$ in $\chi_{\perp c}''(\omega, T)$ plot also. The least-squares fits for the two transitions using the Vogel-Fulcher law are shown using the continuous solid line in these figures. The best fit parameters for the two transitions are: T_{VF}'' = (31.63 ± 0.06) K, τ_0 =(9.8 ± 1) x 10^{-5} s, E_a = (0.63 ± 0.01) meV with GoF = 0.989 and T_{VF}'' = (3.11 ± 0.02) K, τ_0 = (1.3 ± 0.1) x 10^{-4} s, E_a = (0.14 ± 0.002) meV with a GoF =

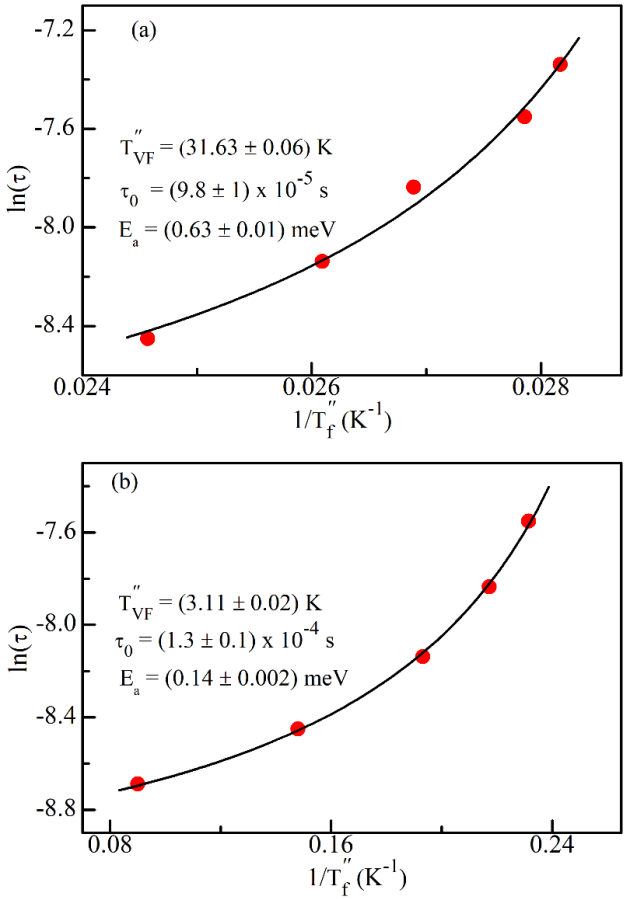

Figure 5.5: The ln(τ) *vs* $1/T_f''$ plots for the (a) higher and (b) lower temperature transitions obtained from the $\chi_{\perp c}''(\omega, T)$ data. The solid line is the least-squares fit for the Vogel-Fulcher law for the two transition with the best fit parameters given along with the figures.

0.998 for the higher and lower temperature transitions, respectively.

To verify the power-law fit, we followed the procedure discussed earlier for the analysis of $\chi'(\omega, T)$ data. The variation of the variance (σ) as a function of T''_{SG}, where the double prime superscript has been used to indicate that these characteristic temperatures were obtained from the $\chi''_{\perp c}(\omega, T)$ plots, shown in Figs. 5.6(a) and (b). These plots reveal minima at T''_{SG} = (33.5 ± 0.1) K and T''_{SG} (4.17 ± 0.01) K corresponding to the higher and lower temperature spin-glass transitions, respectively. The uncertainty of ± 0.1 K and ± 0.01 K for the two critical spin-glass transition temperatures corresponds to the smallest interval at which we chose T_{SG} values to determine the optimum one with lowest variance. For these two values of T''_{SG}, we obtained excellent least squares fit for the ln(τ) vs ln((T''_f - T''_{SG})/ T''_{SG}) plots with the best fit parameters as τ_0 = (5.7 ± 0.3) x 10^{-5} s, zν = (0.85 ± 0.04) with GoF = 0.992 and τ_0 = (1.94 ± 0.07) x 10^{-4} s, zν = (0.3 ± 0.01) with a GoF = 0.995 for the higher and lower temperature transitions, respectively, as can be seen from Figs. 5.7(a) and (b). Thus both Vogel-Fulcher and power laws give excellent fits

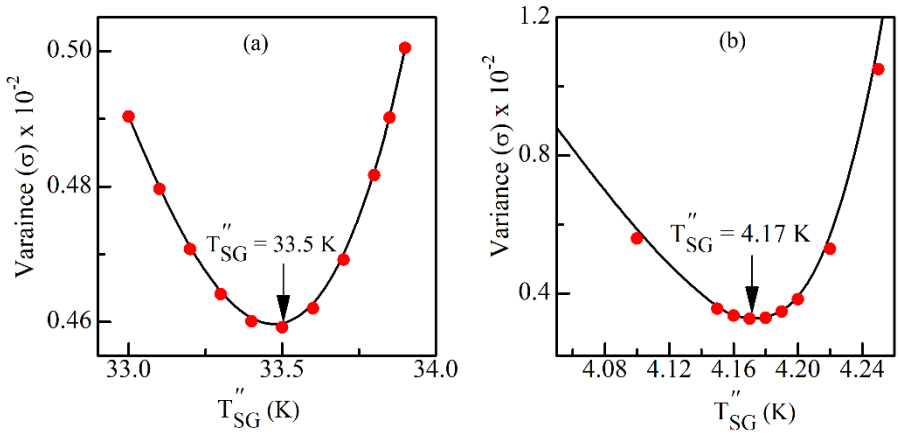

Figure 5.6: Optimization of T''_{SG} for (a) the higher temperature and (b) the lower temperature transitions. The minimum in the two curves gives the optimised critical spin-glass transition temperatures which are indicated with an arrow in each figure.

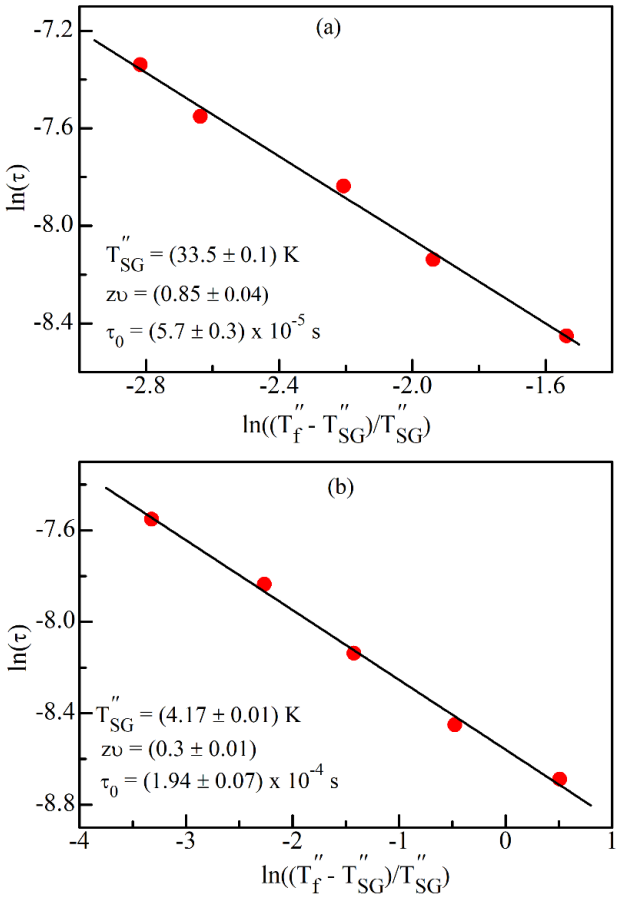

Figure 5.7: The ln(τ) vs ln((T_f'' − T_{SG}'')/T_{SG}'') plots for the power law type spin dynamics for the (a) higher and (b) lower temperature spin-glass transitions seen in $\chi''_{\perp c}(\omega, T)$ data. The best fit parameters are listed along with the figures.

confirming the spin-glass character of the two transitions and ruling out SPM blocking process for the two transitions seen in Fig. 5.1(c). Thus, the critical slowing down of the spin dynamics can be established using either the $\chi'(\omega, T)$ data or the $\chi''(\omega, T)$ data.

5.3.2 Evidence for the Freezing of the Longitudinal Component of the Spins

Having presented evidence for two spin-glass transitions related to the freezing of the transverse component of the spins in the ab-plane, we now proceed to show that there are two spin-glass transitions resulting from the freezing of the longitudinal component of the spins along the c-axis also. The signature of these two transitions are seen in the ac susceptibility χ(ω, T) plots of BFO single crystals. Fig. 5.8 depicts a typical variation of

$\chi'_{//c}$ and $\chi''_{//c}$ with temperature at 200 Hz with an ac drive field of 3 Oe applied parallel to c-axis of the crystal. This figure reveals a diffuse anomaly between ~ 125 K and ~ 250 K, highlighted through the dashed base line, in $\chi'_{//c}$(T). The diffuse transition around 200 K is the subject matter of detailed study in chapter 7 using M(T) and χ(ω, T) data on both single-crystal and polycrystalline samples of BFO along with single-crystal neutron diffraction data.

On lowering the temperature below ~ 60 K, the $\chi'_{//c}$ versus T plot in Fig. 5.8 shows a broad peak in the temperature range 2 to ~ 50 K. A magnified view of this peak, shown as inset in Fig. 5.8, reveals that this diffuse peak consists of two peaks due to two transitions around 15 K and 25 K. The variation of the $\chi'_{//c}$ with temperature at various frequencies is shown in Fig. 5.9(a). It is evident from this figure that the temperature T'_f corresponding to the two peaks in $\chi'_{//c}$(ω, T) plot shifts to the higher temperature side suggesting that these transitions may be due to the successive freezing of the longitudinal

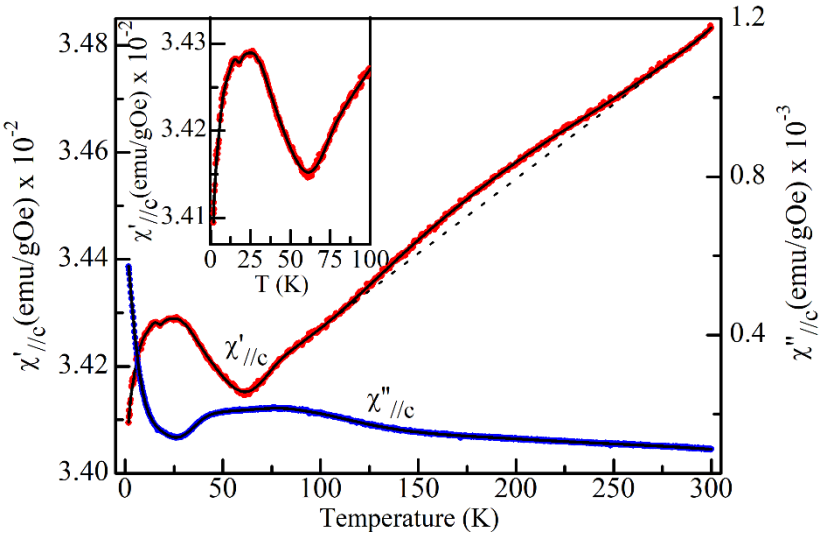

Figure 5.8: Temperature dependence of real $\chi'_{//c}$ and imaginary $\chi''_{//c}$ part of ac susceptibility measured at frequency 200 Hz using ac field of 3 Oe applied along the c-axis of the crystal. Inset shows the variation of $\chi'_{//c}$ on the zoomed scale.

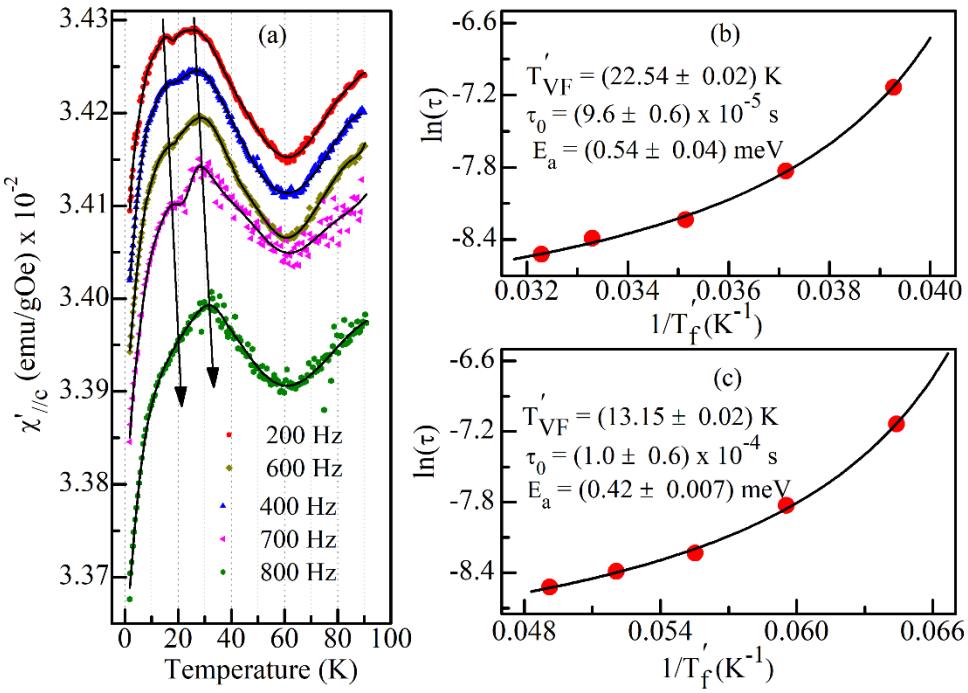

Figure 5.9: (a) Temperature dependence of the real $\chi'_{//c}$ part of ac susceptibility measured at various frequencies using an ac drive field of 3 Oe applied parallel to the c-axis of the crystal. All the curves in (a) are shifted by 0.012 emu/gOe x 10^{-2} along the y-axis and solid continuous line through the data points is a guide to the eyes. The ln(τ) versus $1/T_f'$ plot for the two anomalies are shown in (b) for ~ 25 K and (c) for ~ 15 K transitions observed in $\chi'_{//c}$. The continuous solid line in (b) and (c) is least-squares fit for Vogel-Fulcher law.

component of the spins parallel to the c-axis. We determine the spin relaxation time τ corresponding to each $T_f'(\omega)$ using the realationship $\omega\tau = 1$ where $\omega = 2\pi f$, as discussed already in the previous section.

In order to rule out the Arrhenius type spin dynamics expected for the SPM blocking process, we show in Figs. 5.9(b) and (c) the ln(τ) versus $1/T_f'$ plots for the higher and lower temperature transitions, respectively. The non-linear nature of the ln(τ) versus $1/T_f'$ plots rules out the possibility of SPM blocking being responsible for the frequency dispersion in $\chi'_{//c}(\omega, T)$ and $T_f'(\omega)$ for the two transitions. On the other hand, least-

squares fits using the Vogel-Fulcher law given by Equation (5.3) are excellent for both the plots, as shown in Figs. 5.9(b) and (c) using the continuous line. The corresponding fitting parameters are given in the same figures. The Vogel-Fulcher fit shows the divergence of the spin dynamics at T'_{VF} ~ (22.54 ± 0.02) K and (13.15 ± 0.02) K pointing towards the spin-glass character of these two transitions associated with the freezing of the longitudunal component of the spins.

We also verified critical slowing down of the spin dynamics using $\chi''_{//c}(\omega, T)$ data for the power-law behaviour of τ (Equation (5.4)). The optimum values for the T'_{SG} were obtained using the procedure explained earlier for the transverse conponent. The corresponding variation of the variance with various chosen values of T'_{SG} gives the lowest variance for T'_{SG} = 24.78 K and T'_{SG} = 14.93 K for the two transitions (see Fig. 5.10). The excellent fit between ln(τ) versus ln((T'_f - T'_{SG})/ T'_{SG}) plots for both the transitions using the optimised values of T'_{SG}, shown using continuous solid lines in Figs. 5.11(a) and (b), confirms the divergence of relaxation time τ at the repective T'_{SG} values. The parameters obtained after least-squares fit to the power-law are T'_{SG} = (24.78 ± 0.02)

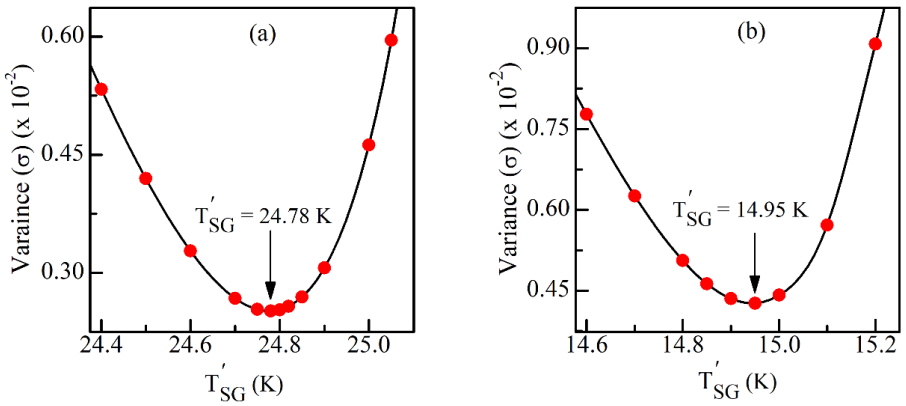

Figure 5.10: Optimization of T'_{SG} for (a) higher and (b) lower temperature transition seen in Fig. 5.9(a).

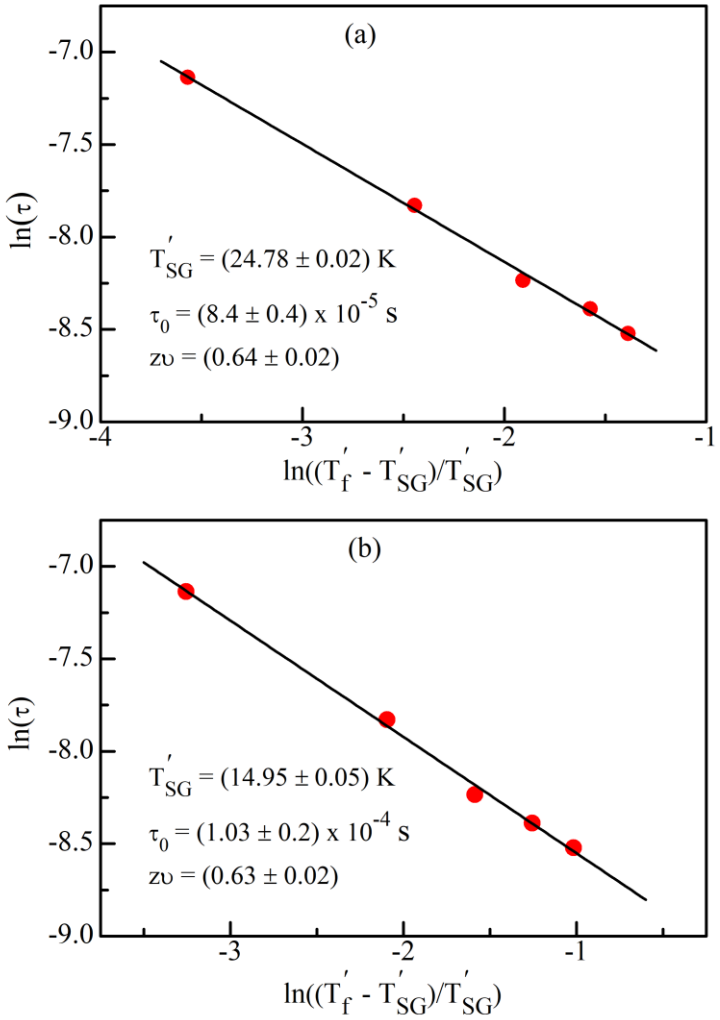

Figure 5.11: The ln(τ) *vs* ln(($T_f' - T_{SG}'$)/T_{SG}') plots along with the least-squares fit for the power law type spin dynamics for the (a) higher and (b) lower temperature transitions seen in $\chi'_{//c}(\omega, T)$ plots in Fig. 5.9(a). The best fit parameters are listed in the two figures.

K, $z\nu$ = (0.64 ± 0.02), τ_0 = (8.4 ± 0.4) x 10^{-5} s with GoF = 0.998 and T_{SG}' = (14.95 ± 0.05) K, $z\nu$ = (0.63 ± 0.02), τ_0 = (1.03 ± 0.2) x 10^{-4} s with GoF = 0.995 for the higher and lower temperature spin-glass transitions, respectively. Thus our $\chi'_{//c}(\omega, T)$ measurements reveals the occurance of two spin-glass transitions due to successive freezing of the longitudinal spin components with spin-glass transition temperatures of T_{SG}' ~ 24.78 K and ~14.95 K.

5.3.3 Signatures of the Spin-Glass Transitions in the Single-Crystal Neutron Diffraction Studies

In this section, we shall present the results of a temperature dependent neutron diffraction study on single crystals of BFO in the temperature range 2 to 300 K with a view to capture the signatures of the four spin-glass transitions discussed in the previous section. Since the integrated intensity of the Bragg peaks is proportional to the square of the ordered magnetic moment, any disordering of the spin components along or perpendicular to the c-axis should lead to departure from the expected Brillouin function behaviour for the magnetic moment.

$$\mu = \mu_0 B_J(x), \qquad \text{.....(5.7)}$$

where, $x = \frac{3J}{J+1}\frac{T_c}{T}\frac{\mu}{\mu_0}$, where J is the total angular momentum, μ and μ_0 are the magnetic moments at finite temperature T and T= 0 K, respectively, and B_J is the Brillouin function given as:

$$B_J(x) = \frac{2J+1}{2J}\coth\left(\frac{2J+1}{2J}x\right) - \frac{1}{2J}\coth\left(\frac{1}{2J}x\right), \qquad \text{.....(5.8)}$$

We carried out neutron diffraction measurement along the 00*l* and 10*l* reciprocal lattice rows of the BFO single crystals in the temperature range 2 to 300 K. To capture the signature of the transverse freezing of the spins, we selected one of the 00*l* reflections as it contains information about the component of the magnetic spins in the basal plane. The 10*l* reflections, on the other hand, contain information about freezing of both the longitudinal and transverse spin components.

To study the variation of the integrated intensities of the 00*l* and 10*l* reflections as a function of temperature, we modelled the peak profile of these reflections using back-

to-back two exponential functions, as the time-of-flight peak shapes can be described well using such a function [265]:

$$\text{Peak shape} \quad = \quad I\frac{(AB)}{2(A+B)}[I_1 + I_2], \qquad \text{.....(5.9)}$$

where $$I_1 = \exp\left(\frac{A[AS^2+2(x-X_0)]}{2}\right)\text{erfc}\left(\frac{A[AS^2+(x-X_0)]}{S\sqrt{2}}\right)$$

and

$$I_2 = \exp\left(\frac{B[BS^2+2(x-X_0)]}{2}\right)\text{erfc}\left(\frac{B[BS^2+(x-X_0)]}{S\sqrt{2}}\right),$$

where I is integrated intensity of the peak, A and B are constants for modelling the rising and the decaying parts of the neutron pulse, X_0 is the peak position and S is the standard deviation of the Gaussian part of the peak shape function.

We fitted the above profile function to the observed neutron diffraction profiles of *006* and *101* reflections at various temperatures in the range 2 to 300 K and the fits are shown in Figs. 5.12, and 5.13, respectively, for a few selected temperatures. As evident from these figures, the fits are pretty good at all the temperatures. The temperature variations of the integrated intensity of the 006 and *101* reflections, obtained after the best fit to the peak profile using back-to-back two exponential functions, are shown in Figs. 5.14 and 5.15 respectively.

The temperature variation of the integrated intensity of the *006* reflection (I_{006}), shown in Fig. 5.14(a), reveals flat bottomed dips in the temperature range 5 to 15 K and 45 to 60 K. This is shown more clearly in the magnified view given in Fig. 5.14(b). The highest temperature anomaly below 175 K is the subject matter of discussion in chapter 7 and we focus here on the two lower temperature anomalies only. The two anomalous dips

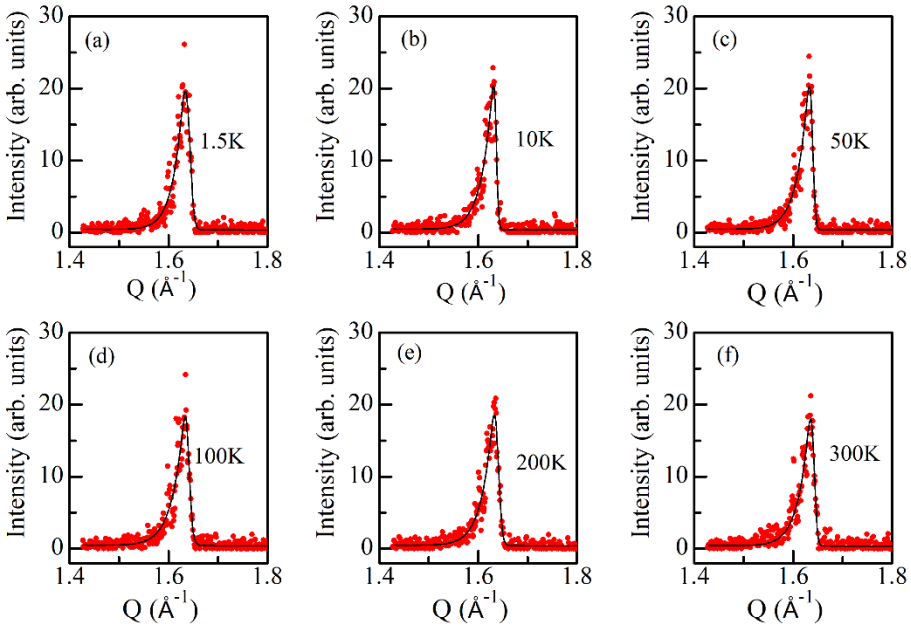

Figure 5.12: Peak profile of *006* Bragg reflection at (a) 1.5 K, (b) 10 K, (c) 50 K, (d) 100 K, (e) 200 K and (f) 300 K: The continuous solid lines through the data points (filled circles) are the fits for the back-to-back two exponential functions.

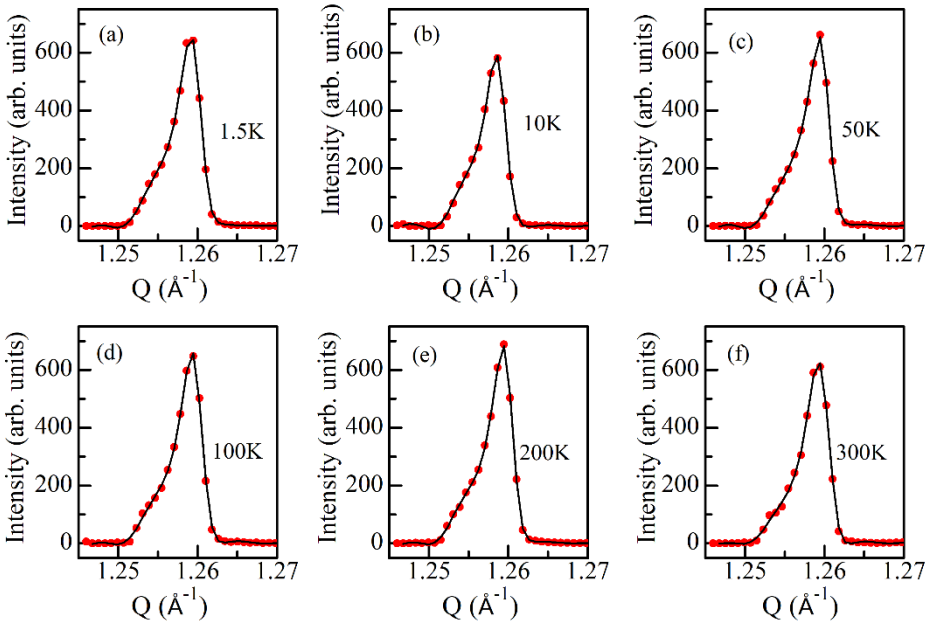

Figure 5.13: Peak profile of *101* Bragg reflection at (a) 1.5 K, (b) 10 K, (c) 50 K, (d) 100 K, (e) 200 K and (f) 300 K: The continuous solid lines through the data points (filled circles) are the fits for the back-to-back two exponential functions.

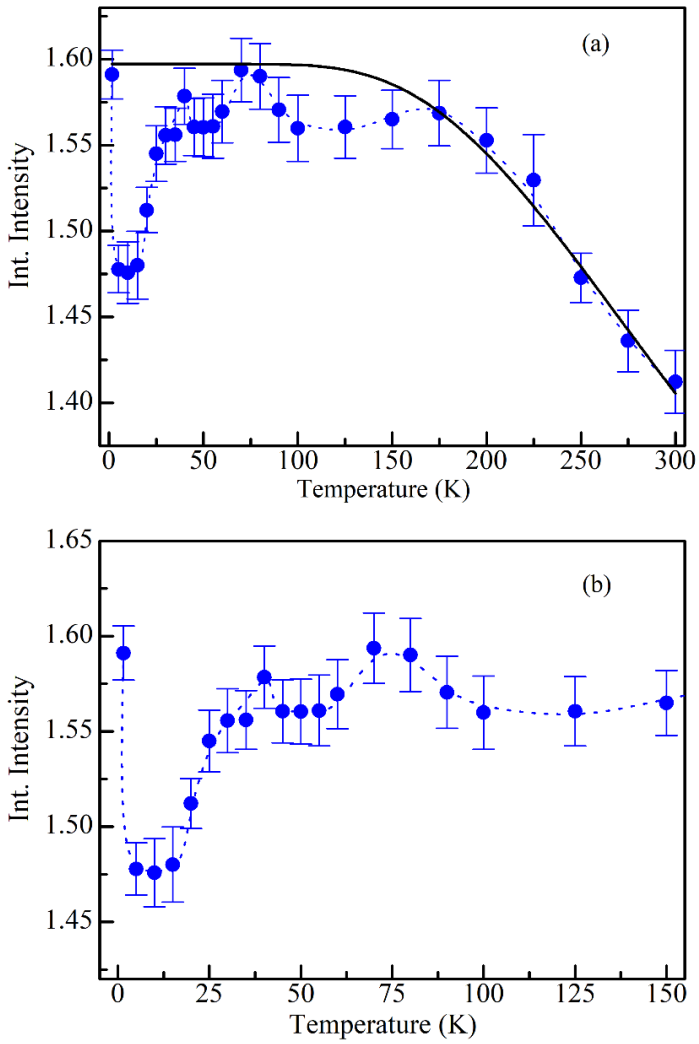

Figure 5.14: Temperature dependence of the integrated intensity of *006* Bragg reflection (a) on the full scale and (b) on the magnified scale, obtained from the neutron diffraction data collected on the single-crystal of $BaFe_{12}O_{19}$. Broken lines in (a) and (b) are guide to the eyes, while the continuous solid line (black coloured) in (a) is the fit for the square of Brillouin function behaviour of μ.

in the temperature dependence of the I_{006} are in the vicinity of the two-transverse spin-glass freezing temperatures whose frequency dependent $T_f'(\omega)$ lies nearly in the same range (see Figs. 5.2(a) and (c)). The fit corresponding to the square of the Brillouin function behaviour (shown using continuous line in Fig. 5.14(a)) shows deviation from

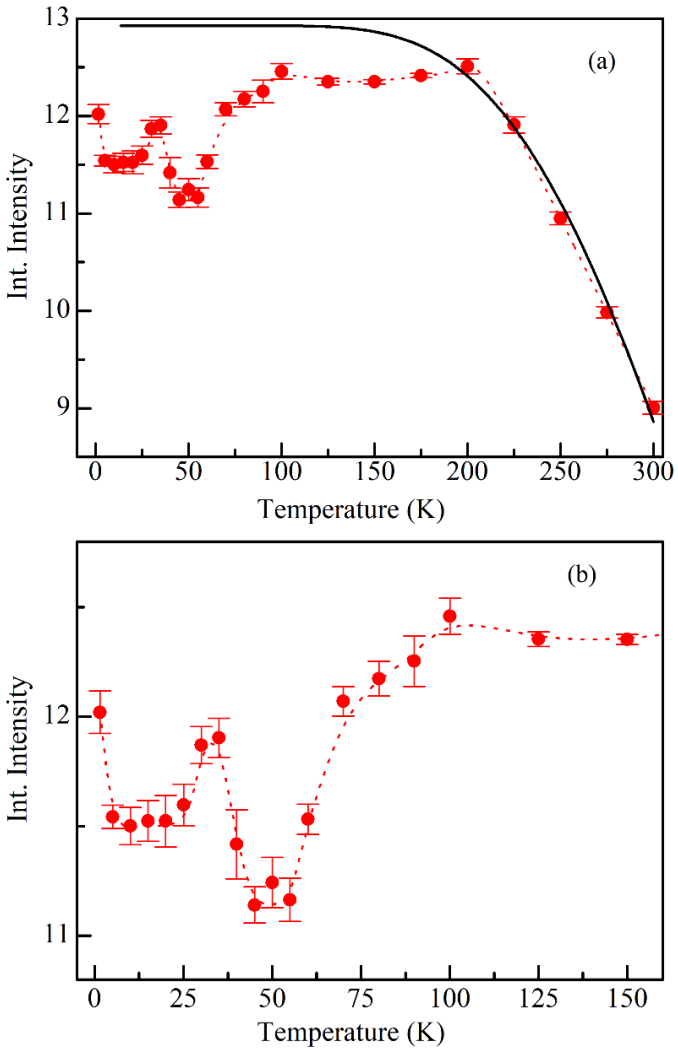

Figure 5.15: Temperature dependence of the integrated intensity of *101* Bragg reflection (a) on the full scale and (b) on the magnified scale, obtained from the neutron diffraction data collected on the single-crystal of $BaFe_{12}O_{19}$. Broken lines in (a) and (b) are guide to the eyes, while the continuous solid line (black coloured) in (a) is the fit for the square of Brillouin function behaviour of μ.

the theoretically expected behaviour below 200 K (see Fig. 5.14(a)). For the two lower temperature transitions in the basal plane, the observed intensities are significantly lower than that expected theoretically for the square of the Brilluoin function behaviour. Interestingly, after each dip, the intensity again increases and tries to approach the theoretically expected curve before decreasing again for the next transition. All these

imply that a part of the basal plane component of the spins is detached from the long-range ordered phase and leads to the spin-glass transition as discussed in the literature [74,266] . It is this part of the basal plane spin component that is involved in the freezing associated with the two spin-glass transitions observed perpendicular to the c-axis in Fig. 5.2 similar to that in Ref. [74] and [266] for two different disordered systems.

The integrated intensity of the 101 (I_{101}) reflection also shows deviation from the expected square of the Brilluoin function behaviour in the temperature range 5 K to 25 K, 45 K to 55 K and 100 K to 175 K (see Fig. 5.15(a)). Our focus in this chapter is on the lower temperature dips, as the highest temperature dip is the subject matter of chapter 7. The anomalous behaviour of I_{101} shown more clearly in Fig. 5.15(b) in the vicinity of the transverse spin-glass freezing temperature is in agreement with the temperature variation *006* reflection. The spin-glass freezing temperatures $T_f(\omega)$ for the remaining three transitions are very close by. The freezing of the transverse component of the spins at the lowest temperatures occurs in the temperature range ~ 4 K to ~ 11 K, whereas the two longitudinal freezing occur in the temperature range ~ 15 K to ~ 31 K. The broad flat-bottomed dip in the 5 to 25 K range contains the signature of all the three transitions. It is worth mentioning that the flat-bottomed dip in Fig. 5.14(b) for the *006* reflection extends from ~ 5 K to ~ 10 K only whereas the lower temperature dip in *101* reflection extends from ~ 5 K to ~ 25 K. The increase in the temperature range of that bottomed dip which comes in the range $T_f(\omega)$ for the two transitions involving the longitudinal component of the spins.

The presence of the two dips in Figs. 5.14 and 5.15 demonstrates that only a part of the ordered magnetic moments along and perpendicular to the c-axis are involved in the spin-glass freezing while the remaining parts remain ordered suggesting coexistence of the spin-glass and the ferrimagnetic phases.

We also attempted to capture the signatures of the four magnetic transitions of BFO below room temperature in the specific heat (C_P) studies on BFO powder. The variation of C_P with temperature shown in Fig. 5.16 in the 1.8 K to 300 K range does not as such reveal signature of any transition. However, the same data when plotted in different formats reveals clear signatures of all the four transitions. For example, the C_P/T versus T^2 plot shown in Fig. 5.17 on a semi-log scale reveals the appearance of a diffuse peak over the monotonically decreasing background (shown with red line in the figure) with an onset temperature of ~ 15 K which is close to the T_{SG} of the lowest temperature longitudinal spin-glass transition (see inset (i) also). The signature of the next longitudinal spin-glass transition in this plot is not so clear except for the fact that the experimental values deviate from the trend of the C_P/T versus T^2 curve shown with blue line at ~ 25 K, as shown more clearly in inset (ii). The huge diffuse peak around 170 K is due to conical spin-glass phase discussed in chapter 7. This peak seems to overwhelm the signature of the first longitudinal spin-glass transition. The signature of the two-transverse spin-glass

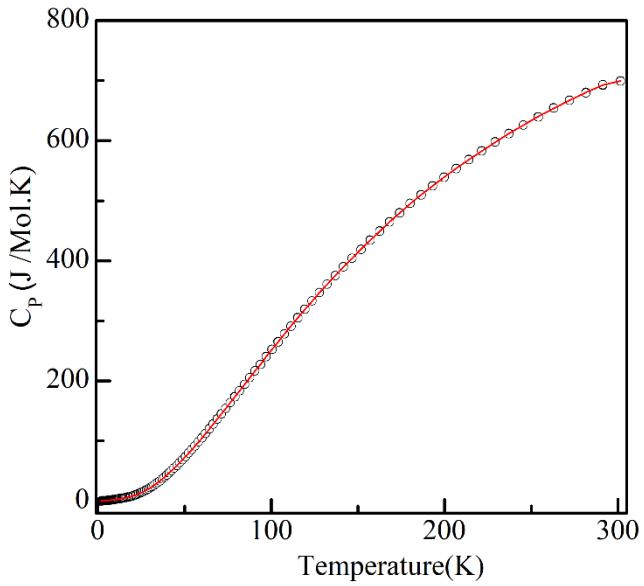

Figure 5.16: Variation of C_P with temperature (T).

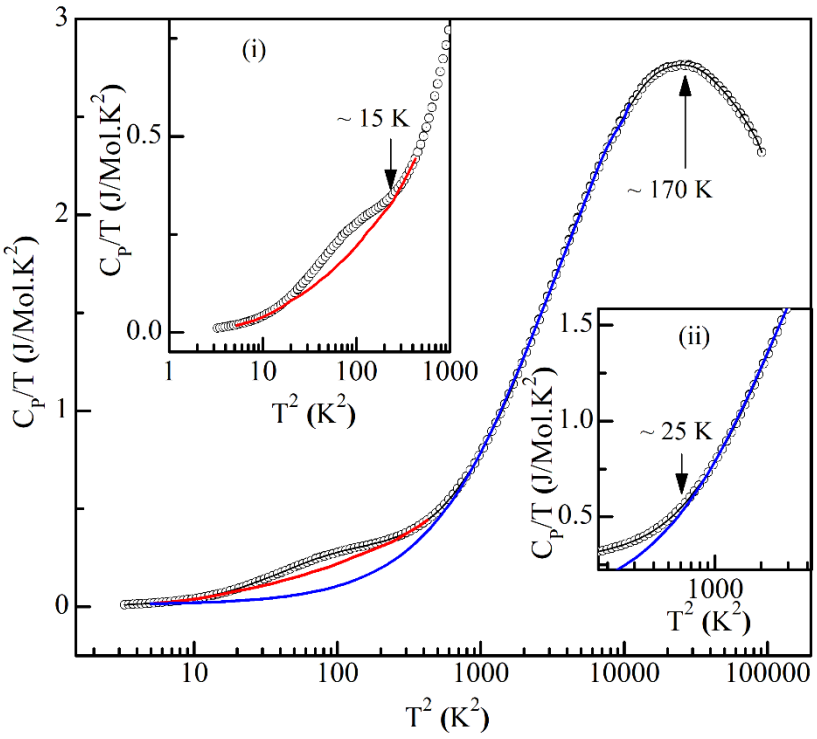

Figure 5.17: Variation of C_P/T with square of the temperature (T).

transitions are revealed in the C_P/T^3 versus T plot shown in Fig. 5.18. The lowest temperature peak in this figure at ~ 2.7 K is due to the quantum electric dipole liquid state discussed later on in chapter 9. The second peak occurs around 5 K which is close to the lowest temperature transverse spin-glass transition temperature. The signature of the second transverse spin-glass transition is also seen in this figure as a hump around 50 K. Thus, the specific heat data also confirms all the four spin-glass transitions discussed in this chapter. The C_P/T^3 versus T plot is often used to locate the Boson peak at low temperatures (< 20 K) in liquids and glassy materials [267,268,277–285,269–276]. It represent excess specific heat due to non-Debye contributions from low energy localised excitations [269,271,282–285,273,275–281]. However, this explanation is not valid for the peaks seen at the four spin-glass transitions. We believe that the anomalies seen in various representations of specific heat plots around the spin-glass transitions temperatures may be due to the coupling of the spin, lattice [137,138,160] and charge

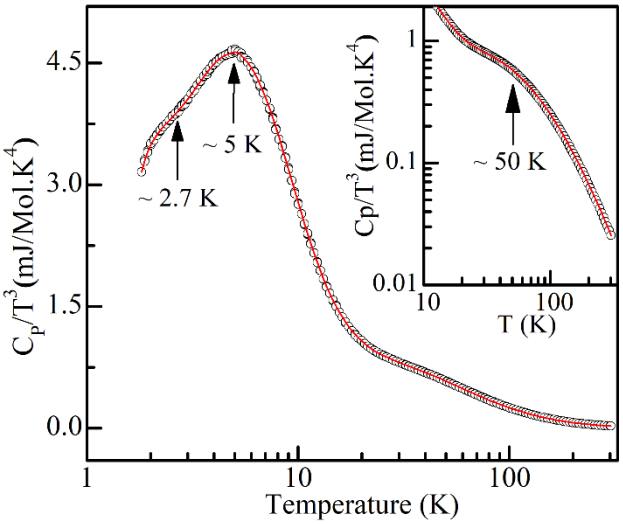

Figure 5.18: Variation of C_P/T^3 with temperature (T).

degrees of freedom leading to new excitations like electromagnons [286]. Inelastic neutron and X-ray scattering measurements [271,287,296,297,288–295] along with Raman scattering studies [137,138,160] backed up by appropriate theoretical modelling is required to understand the genesis of the signature of spin-glass transitions in C_P/T^3 versus T and C_P/T versus T^2 plots.

5.3.4 The Outlook

In the foregoing, we have presented evidence for two spin-glass transitions each associated with the freezing of the transverse and longitudinal components of the spins. Table 5.1 summarises the characteristic values for the T_{VF}, τ_0 and activation energy E_a for the Vogel-Fulcher fits and T_{SG}, $z\nu$ and τ_0 for the power-law fits for the four spin-glass transitions. Except for the lowest temperature spin-glass transition, all the values in this Table correspond to the fits obtained using frequency dependent peak temperatures $T_f'(\omega)$ in $\chi'_{\perp c}(\omega, T)$. For the lowest temperature transition, we used the $T_f''(\omega)$ corresponding to the peak in $\chi''_{\perp c}(\omega, T)$ as it was not possible to locate the corresponding peak in $\chi'_{\perp c}(\omega, T)$

curve. Use of $T_f''(\omega)$ gives lower values of T_{VF}/T_{SG} as compared to those obtained using $T_f'(\omega)$, as demonstrated for the highest temperatures transition in the $\chi_{\perp c}(\omega, T)$.

It is interesting to note that both the Vogel-Fulcher and power-law fits give values of τ_0 of the order of 10^{-4} s. For the atomic spin glasses, this value is of the order of 10^{-12} to10^{-13} s as it involves flipping of isolated spins [57–61,245–247,298,299]. The fact that τ_0 for all the four spin-glass transitions in BFO are much larger suggests that the spin dynamics in these transitions involve spin clusters and not isolated spins. For cluster spin glasses, such large τ_0 value are commonly observed [75,300,309–312,301–308]. Presence of spin clusters in geometrically frustrated ordered compounds undergoing spin-glass transition has been reported using small angle neutron scattering [313] and diffuse neutron scattering studies [257,314]. As shown in chapter 8, BFO also exhibits geometrical frustration due to the emergence of kagome spin configurations as a function of temperature and we believe that the large τ_0

Table 5.1: List of parameters obtained after least-square fit to the Vogel-Fulcher and power-law dynamics to spin relaxation time.

Transitions in $\chi(\omega, T)$	Fitting parameters for Vogel-Fulcher law				Fitting parameters for power-law			
	T_{VF} (K)	τ_0 (s)	E_a (meV)	GoF	T_{SG} (K)	τ_0 (s)	zν	GoF
1	3.11 ± 0.02	(1.3 ± 0.1) x 10^{-4} s	(0.14 ± 0.002)	0.998	4.17 ± 0.01	(1.94 ± 0.07) x 10^{-4}	0.30 ± 0.01	0.995
2	13.15 ± 0.02	(1.0 ± 0.6) x 10^{-4}	(0.42 ± 0.007)	0.998	14.95 ± 0.05	(1.03 ± 0.2) x 10^{-4}	0.63 ± 0.02	0.995
3	22.54 ± 0.02	(9.6 ± 0.5) x 10^{-5}	(0.54 ± 0.04)	0.998	24.78 ± 0.02	(8.4 ± 0.4) x 10^{-5}	0.64 ± 0.02	0.998
4	45.46 ± 003	(1.8 ± 0.1) x 10^{-4}	(0.13 ± 0.006)	0.995	46.035 ± 0.005	(8.2 ± 0.8) x 10^{-5}	0.50 ± 0.02	0.990

is related to the presence of local spin clusters due to macroscopic degeneracy of the kagome spin configuration of BFO, similar to those observed in other ordered compounds.

Interestingly, the critical freezing temperature T_{VF} and T_{SG} as obtained from the Vogel-Fulcher and power-law fits are quite close to each other. In fact, they are more close to each other for the transverse components than for the longitudinal component. Further, the activation energy E_a for Vogel-Fulcher law are quite close to each other within (0.5 ± 0.1) meV range, except for the lowest temperature transition for which $E_a \simeq$ 0.14 meV. We believe that the lowest temperature transition may be affected by quantum fluctuations also, as discussed in chapter 9 in relation to quantum electric dipole liquid and dipole glass transitions.

The calculated $z\nu$ value for BFO is anomalously small. Conventionally the values of exponent $z\nu$ lies between 4 and 12 for spin glasses [60]. However, several disordered oxides and alloy-based systems have been reported to exhibit low $z\nu$ values in the range $2 < z\nu < 4$ [249,300,315–317], $1 \leq z\nu < 2$ [302,311,317–320] and $z\nu < 1$ ($z\nu = 0.9$, & 0.55) [321,322]. Currently, there is little theoretical understanding of such unconventional exponents even in disordered systems, except suggesting that the $z\nu \geq 4$ for 3D systems [323,324] and $z\nu < 4$ for 2D systems [323]. In the absence of any theoretical insights into these unconventionally low values of exponents, such spin glasses have been termed as unconventional spin glasses [321].

The spin-glass transition has conventionally been linked with substitutional site-disorder that is responsible for the frustration and the randomness of the interactions [57,60,61,325,326]. In this context, the observation of spin-glass transition in an ordered compound like BFO without any substitutional disorder appears intriguing. However, spin-glass transition has been reported in several geometrically frustrated

ordered compounds like pyrochlores (e.g., $Tb_2Mo_2O_7$) [327–335], hydronium jarosites (e.g., $(H_3O)Fe_3(SO_4)_2(OH)_6$) [336], spinels (e.g., MAl_2O_4 with M=Co, Fe, and Mn) [312,337–339] and hexagonal-$DyMnO_3$ [249]. Recent theoretical studies on spin-glass transition in geometrically frustrated ordered compounds suggest that the presence of an infinitesimal disorder due to anisotropic exchange interactions or magnetoelastic strains is sufficient to bring in randomness in the interactions and thereby stabilize the spin-glass state [332,340–347]. We shall return to this aspect in chapter 8 where we present evidence for the emergence of kagome spin configurations and magnetoelastic strains below room temperature in BFO.

The spin-glass phase reported in the geometrically frustrated compounds including BFO is different from those reported in $CaBaFe_4O_{7+\delta}$ [348], $GaFeO_3$ [349], Mn_3In [350] and $Na_2Mn_3(SO_4)_3(\mu_3\text{-}OH)_2(\mu_2\text{-}OH_2)_2$ [351] like compounds where there is inherent cation disorder due either to mixed-valence states or anti-site disorder or randomness in the partial occupancy of the Wyckoff position. For example, in $CaBaFe_4O_{7+\delta}$, there is cation disorder due to the presence of Fe^{3+} and Fe^{2+} for $\delta < 1$ [348]. Similarly, there is mixed occupancy at the octahedral site by Fe^{3+} and Ga^{3+} in $GaFeO_3$ [349]. In Mn_3In, there is mixed occupancy at both the octahedral and cubo-octahedral sites by Mn and In [350]. In $Na_2Mn_3(SO_4)_3(\mu_3\text{-}OH)_2(\mu_2\text{-}OH_2)_2$, there is a disorder in the position of Mn ion as only 3/2 sites in the asymmetric unit are occupied randomly by Mn ion [351]. In our case, no disorder was introduced by modifying the oxygen stoichiometry deliberately, as was done in the case of $CaBaFe_4O_{7+\delta}$. Also, mixed occupancy by Ba^{2+} and Fe^{3+} is not possible due to the large difference in their ionic radii in the nearly close-packed structure of BFO. In view of these, the spin-glass transitions in BFO are of different origin than in the compound listed above.

BFO is isostructural with SCGO where a kagome bi-layer configuration of the spins has been reported for the basal plane spins. We believe that the formation of kagome bi-layer configuration for the basal plane component of the spins in BFO (as confirmed in chapter 8) along with the anisotropy in the exchange interactions as well as variation in the exchange interactions due to nearest neighbour distances due to magnetoelastic strains is responsible for the stabilization of the spin-glass phase observed by us in BFO. This aspect will be discussed further in chapter 8. However, we would like to emphasise that the analogy with SCGO and other geometrically frustrated ordered compounds like $Tb_2Mo_2O_7$ [334], MAl_2O_4 [337] and $(H_3O)Fe_3(SO_4)_2(OH)_6$ [336] is not exact in relation to BFO. Only one spin-glass transition emerges directly from the paramagnetic phase in all these geometrically frustrated ordered compounds whereas BFO exhibits multiple spin-glass transition resulting from successive freezing of transeverse and longitudinal spin components of the $3d^5Fe^{3+}$ spins in the LRO ferrimagnetic phase of BFO, which continues to coexist with the spin-glass phase in BFO. In this respect, the discovery of successive spin-glass transitions in BFO aquires special significance.

5.4 Conclusions

(1). We have discovered four successive spin-glass transitions in BFO whose spin dynamics diverges at T_{SG} ~ 46 K, ~ 25 K, ~ 15 K and ~ 4 K. The spin dynamics which can be modelled by both Vogel-Fulcher and power-laws. This is the first experimental report of four spin-glass transitions in an ordered system emerging from a LRO magnetic phase unlike the other geometrically frustrated pyrochlores, spinels where only one spin-glass resulting directly from the paramagnetic phase has been reported.

(2). We have presented signatures of the observed spin-glass transitions using temperature-dependent single-crystal neutron diffraction studies. The anomalous

behaviour of the integrated intensity of *006* and *101* reflections in the vicinity of the T_{SG} (~ 4 K, ~ 15 K, ~ 25 K and ~ 46 K) validates the presence of the spin-glass phases in coexistence with the long-range ordered ferrimagnetic phase.

(3). The attempt spin relaxation time is rather large (~ 10^{-4} s) suggesting the involvement of spin clusters similar to those observed in other geometrically frustrated compounds [301,310,312]. The exponent *zv* is found to be less than 1 and corresponds to unconventional spin glasses reported in the literature.